
CMS Physics Analysis Summary

Contact: cms-pag-conveners-smp@cern.ch

2013/06/26

Measurement of the ratio of inclusive jet cross-sections with radius parameters $R = 0.5$ and $R = 0.7$ using the anti- k_T algorithm at $\sqrt{s} = 7$ TeV

The CMS Collaboration

Abstract

Measurements of the inclusive jet cross section with the anti- k_T clustering algorithm are presented for two radius parameters, $R = 0.5$ and $R = 0.7$. The data from LHC proton-proton collisions at $\sqrt{s} = 7$ TeV, corresponding to 5.0 fb^{-1} of integrated luminosity, have been collected with the CMS detector. The ratio of the two measurements is derived as a function of the rapidity and transverse momentum of the jets. Significant discrepancies are found comparing the data to LO simulations and to fixed order calculations at NLO, corrected for non-perturbative effects, whereas simulations with NLO matrix elements matched to the parton showers describe the data quite well. This result is an indication of the importance of final state radiation in the description of the inclusive jet cross section with small radius parameter such as $R = 0.5$.

1 Introduction

Quantum Chromodynamics (QCD) is a gauge group theory that describes the strong interaction between quarks and gluons. The production cross section of events with high transverse momentum jets ($p_T \gg 1$ GeV) in hadron or lepton colliders is described by QCD in terms of parton-parton scattering. The standard way to compute the cross section is $\sigma_{\text{jet}} = \sigma_n \times f_{\text{NP}}$, where the perturbative component σ_n is obtained at a fixed order n using the factorization theorem, while the non-perturbative component of the cross section is accounted for by an effective factor f_{NP} .

The order of the calculations n is defined with respect to the tree level process under consideration and is limited by the complexity of the calculations and the specific structure of the infrared divergences of the QCD radiation. For lepton-proton collisions (*e.g.* HERA), proton-antiproton collisions (*e.g.* Tevatron) and proton-proton collisions (*e.g.* LHC), the next-to-leading-order (NLO) calculations are available using programs such as NLOJET++ [1], while for 3-jet production in electron-positron collisions at LEP even next-to-next-to-leading-order (NNLO) calculations are available, taking advantage of the fact that the initial state particles do not carry a color charge [2, 3].

The impact of the missing orders is estimated by looking at the residual dependence of the perturbative cross section on the renormalisation (μ_r) and factorization scales (μ_f). The fundamental renormalisation theory of QCD predicts that the dependence on those scales will vanish with the increasing order of the perturbative calculations. A clever choice of those scales, usually related to physical quantities such as p_T , may improve the speed of the convergence of the perturbative series. The variation range is arbitrary, but the choice of factors 0.5 and 2 has been shown to cover the differences observed between data and theory at HERA [4, 5].

The non-perturbative (NP) correction factors include the fragmentation and confinement smearing effects and the underlying event that is produced by the color-charged proton remnants, which is not directly related to the hard-scattering process. They are usually taken from Monte Carlo (MC) simulations where the multi-parton topologies are generated at tree level and the missing orders are generated through a parton shower model such as PYTHIA [6], HERWIG [7], etc. The produced partons are then hadronized using semi-empirical models such as the string fragmentation [8] or cluster models [9].

The final ingredient of a well-defined jet cross section is the choice of the jet algorithm, which should be both infrared and collinear safe. The sequential recombination algorithms, such as k_T [10] and anti- k_T [11], fulfill these conditions. The only free parameter in this kind of algorithm is the clustering parameter R , also referred to as jet radius for the anti- k_T algorithm. The choice of the clustering parameter defines the typical size of the jet in the y - ϕ space.

The above-mentioned approach, denoted henceforth as $\text{NLO} \otimes \text{NP}$ (or $\text{NNLO} \otimes \text{NP}$) has been shown to be a good description of the multijet production at LEP and HERA [4, 5]. In this latter case the typical scale was of the order of 50 GeV and the k_T algorithm was used with the R parameter varying between 0.5 and 1 [5].

The inclusive jet measurements at the Tevatron [12–15] are in also good agreement with the predictions. They were performed with the midpoint cone algorithm with $R_{\text{cone}} = 0.7$ [16], which corresponds roughly to $R = 1$ in the case of the k_T algorithm [17], or directly with the k_T algorithm with radius parameter $R = 0.7$.

The inclusive jet production at the LHC has been measured by CMS [18–20] and ATLAS [21] at the center of mass energy $\sqrt{s} = 7$ TeV and by ATLAS [22] and ALICE [23] collaborations

at $\sqrt{s} = 2.76$ TeV. These measurements have been done using the anti- k_T algorithm with R choices of 0.2 and 0.4 (ALICE), 0.4 and 0.6 (ATLAS), and 0.5 and 0.7 (CMS). While the measurements with $R \geq 0.4$ agree with NLO \otimes NP predictions within experimental and theoretical uncertainties, there is slight tendency for better agreement with larger jet radii.

Some indication about the nature of this tendency appears when the measured cross section is compared to the POWHEG prediction [24] shown by the ATLAS collaboration [21]. The POWHEG MC program matches NLO matrix element predictions for dijet production with the parton showers and exhibits improved agreement with the data. Analyses of the azimuthal decorrelation between the two leading jets in the central region ($|y| < 0.8$ and $|y| < 1.1$ for ATLAS and CMS, respectively) [25, 26] show the importance of initial state radiation (ISR) to properly describe the rate of decorrelated events with $\Delta\phi_{\text{jet1-jet2}} \approx \pi/2$. The jet shape measurements by CMS [27] and ATLAS [28] show differences between data and various parton shower models and MC generator tunes. These observations seem to point towards the importance of collinear emission at hadron colliders. A larger radius tends to capture more of this radiation, making the calculation less sensitive to its details.

This analysis is dedicated to the study of the impact of collinear radiation in the final state (FSR) on the inclusive jet cross section. The ratio of the jet cross section with $R = 0.5$ to that of $R = 0.7$, referred to as the jet radius ratio, $\mathcal{R}(0.5, 0.7)$, is measured as a function of the jet p_T and the rapidity y .

2 Detector

A detailed description of the Compact Muon Solenoid (CMS) experiment can be found elsewhere [29]. The CMS coordinate system has the origin at the center of the detector. The z -axis points along the direction of the anti-clockwise beam, with the transverse plane perpendicular to the beam; ϕ is the azimuthal angle, θ is the polar angle, pseudorapidity is defined as $\eta \equiv -\ln(\tan[\theta/2])$.

The central feature of the CMS apparatus is a superconducting solenoid, of 6 m internal diameter, providing a field of 3.8 T. Within the field volume are a silicon pixel and strip tracker, a crystal electromagnetic calorimeter (ECAL) and a brass/scintillator hadron calorimeter (HCAL). The ECAL is made up of lead-tungstate crystals, while the HCAL is made up of layers of plates of brass and plastic scintillator. These calorimeters provide coverage in pseudorapidity up to $|\eta| < 3.0$. An iron or quartz-fiber Čerenkov hadron calorimeter (HF) covers pseudorapidities $3.0 < |\eta| < 5.0$. The muons are measured in the pseudorapidity range $|\eta| < 2.4$, with detection planes made using three technologies: drift tubes, cathode strip chambers, and resistive plate chambers. Matching the muons to the tracks measured in the silicon tracker results in a transverse momentum resolution between 1 and 5 %, for p_T values up to 1 TeV. The ECAL has an energy resolution of better than 0.5 % for unconverted photons with transverse energies above 100 GeV. The HCAL, when combined with the ECAL, measures jets with a resolution $\Delta E/E \approx 100\%/\sqrt{E [\text{GeV}]} \oplus 5\%$.

3 Monte Carlo models and theory calculations

This section describes the various MC generators and theory calculations used in this analysis.

PYTHIA 6.422 [6] uses leading order (LO) matrix elements to generate the $2 \rightarrow 2$ hard process in perturbative QCD (pQCD) and a parton shower model to simulate higher order processes [30–32]. The parton shower model gives a good description of parton emission when the emitted

partons are close in phase space. Events were generated with tune Z2 for the underlying event. The Z2 tune is identical to the Z1 tune described in [33], except that Z2 uses the CTEQ6L1 [34] parton distribution functions. Parton showers are ordered by p_T . Hadronization is simulated using the Lund string model [35, 36].

The HERWIG++ [7] Tune 2.3 program takes LO matrix elements and simulates parton showers using the coherent branching algorithm with angular ordering of showers. In the formation of hadrons from the quarks and gluons produced in the parton shower, the cluster hadronization model is used. The underlying event is simulated using the eikonal multiple partonic scattering model.

POWHEG [24] is a general computing framework for implementing NLO calculations in MC programs according to the method implemented in the POWHEG BOX package [37, 38] and allows one to use either PYTHIA or HERWIG + JIMMY [39] to shower the partons, hadronize them, and to model the underlying event.

While PYTHIA and HERWIG++ are used for the unfolding of data, all three generators are compared at the particle level to the jet radius ratio. The dependence on the jet radius ratio is generated in HERWIG and PYTHIA only through the parton showering while in POWHEG it appears already on the level of the matrix elements.

The fixed order predictions are shown in Fig. 4. The LO prediction of the jet radius ratio is obtained using NLOJET++ program (v2.0.1) [1] within the framework of the fastNLO package (v1.4) [40]. The NLO calculations are performed using the prediction from [41]. The non-perturbative correction factors are estimated from PYTHIA and HERWIG as in [19].

4 Measurement of differential jet cross sections

The measurement of the jet radius ratio is done by performing two measurements of the differential jet cross sections with anti- k_T clustering parameters $R = 0.5$ and $R = 0.7$. The measurements are reported for $p_T > 56$ GeV in six 0.5-wide bins of absolute rapidity for $|y| < 3.0$. The methods used in this paper closely follow those presented in Ref. [19] for $R = 0.7$, and the results fully agree with the earlier publication within the overlapping phase space. The results for $R = 0.5$ also agree with the earlier CMS publications [42] within statistical and systematic uncertainties. Particular care was taken to ensure that any residual biases in the $R = 0.5$ and $R = 0.7$ measurements would cancel for the jet radius ratio, whether coming from the jet energy scale, jet resolutions, unfolding, trigger or luminosity. The statistical correlations between the two measurements are directly determined from data, and are propagated to the final uncertainty estimates for the jet radius ratio \mathcal{R} .

4.1 Data samples and event selection

The jets were reconstructed using the four-momentum vectors of the reconstructed particle candidates. Each such candidate is constructed using the particle-flow technique [43], which combines information from several subdetectors and is calibrated to account for the nonlinear and nonuniform response of the CMS calorimeters to hadrons. The reconstructed jets require a small additional energy correction, mostly due to thresholds on reconstructed tracks and clusters in the particle-flow algorithm, and various reconstruction inefficiencies [44].

Events were collected online with a two-tiered trigger system, consisting of a hardware level-1 (L1) and a software high level trigger (HLT). The jet algorithm is run by the L1 trigger using the energies measured in the ECAL, HCAL, and HF detectors. The anti- k_T clustering [45] with

Table 1: The nominal trigger p_T thresholds and corresponding thresholds used for analysis and effective integrated luminosity.

Nominal trigger p_T threshold (GeV)	30	60	110	190	240	300
Minimum p_T for analysis (GeV)	56	97	174	300	362	507
\mathcal{L}_{eff} (pb^{-1})	0.0149	0.399	7.12	150	513	4961

the radius parameter $R = 0.5$ is used as implemented in the FASTJET package [46]. The data samples used for this measurement were collected with single-jet high-level triggers (HLT) that require at least one jet in the event to have p_T exceeding a minimal value roughly equivalent to the nominal trigger p_T listed in Table 1. This minimal value has been periodically increased to account for increasing instantaneous luminosity.

For each trigger threshold the turn-on curve for the larger radius parameter $R = 0.7$ is less sharp than for $R = 0.5$. The analysis trigger selections ensure more than about 97% (98.5%) trigger efficiency for $R = 0.7$ at $p_T = 56$ GeV ($p_T > 114$ GeV), and better than about 99.5% for $R = 0.5$ at $p_T = 56$ GeV. These selections, which closely follow those reported in Ref. [19], are reproduced in Table 1.

4.2 Reconstruction of the cross section

The jet p_T spectrum is obtained by populating each bin with the number of jets collected using the highest threshold trigger which gives more than 97% trigger efficiency in all rapidity bins for the jet cross section reconstructed using $R = 0.7$. The yields from each trigger path are then scaled according to the effective integrated luminosity, shown in Table 1.

The observed inclusive jet yields are transformed into double-differential cross sections as follows:

$$\frac{d^2s}{dp_T dy} = \frac{1}{\epsilon \cdot \mathcal{L}_{\text{eff}}} \frac{N_{\text{jets}}}{\Delta p_T \Delta y}, \quad (1)$$

where N_{jets} is the number of jets in the bin, \mathcal{L}_{eff} is the integrated luminosity of the data sample from which the events are taken, ϵ is the product of the trigger and event selection efficiencies, and Δp_T and Δy are the transverse momentum and rapidity bin widths, respectively. The width of the p_T bins is proportional to the p_T resolution and so increases with p_T .

Because of the detector resolution and the steeply falling spectra, the measured cross sections s are smeared with respect to the particle-level cross sections σ . The Gaussian smearing functions are obtained from the detector simulation and are then corrected for the measured differences in the resolution between data and simulation [44]. These p_T dependent resolutions are folded with the NLO \otimes NP theory predictions, and are then used to calculate the response matrices for jet p_T . The unfolding is done with the RooUnfold package [47] using the D'Agostini method [48]. The unfolding reduces the measured cross sections by 5–20% (15–30%) for $R = 0.5$ and 5–25% (15–40%) for $R = 0.7$ at $|y| < 2.5$ ($2.5 < |y| < 3$). The large unfolding factor at $2.5 < |y| < 3$ is the result of the steep p_T spectrum combined with the poor p_T resolution outside the tracking coverage. The differences between $R = 0.5$ and $R = 0.7$ at all rapidities are most evident at $p_T < 100$ GeV, and are due to the larger cone of the $R = 0.7$ jets being more sensitive to extra smearing from pile-up.

The unfolding was cross-checked by smearing the NLO \otimes NP theory and using RooUnfold implementation of SVD (singular value decomposition) method, which were both found to be in excellent agreement with the D'Agostini method.

The unfolded jet cross section measurements with $R = 0.5$ and $R = 0.7$ are shown in Fig. 1.

Figure 2 shows the ratio of data to NLO \otimes NP theory prediction, together with previous measurements [19, 42] for comparison. While the data agrees with theory within uncertainties for both jet radii, the agreement is slightly better for $R = 0.7$.

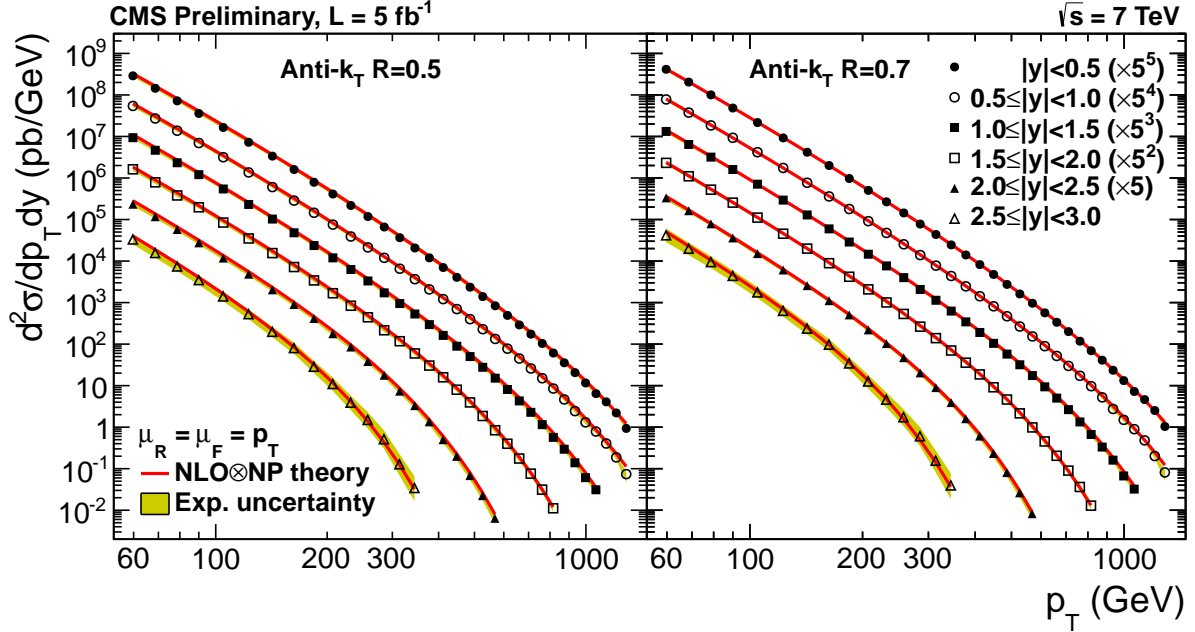


Figure 1: Unfolded inclusive jet cross section with anti- k_T $R = 0.5$ (left) and $R = 0.7$ (right) compared to an NLO \otimes NP theory prediction.

4.3 Measurement of the jet radius ratio

The unfolded cross sections σ_5 and σ_7 for $R = 0.5$ and $R = 0.7$, respectively, are directly divided to calculate the jet radius ratio $\mathcal{R}(0.5, 0.7) = \sigma_5/\sigma_7$, but the statistical uncertainty is calculated separately to account for the correlation between the two measurements.

The procedure below for getting from the data to the jet radius ratio $\mathcal{R}(0.5, 0.7)$ and then to its covariance matrix is as follows: the data are in the form of the jet number cross-sections m_{pq}^{ij} . From these are extracted the jet cross sections s_5 and s_7 as functions of p_T . After unfolding these become σ_5 and σ_7 , from which the jet radius ratio $\mathcal{R}(0.5, 0.7)$ is extracted for each p_T bin.

For the errors, the W matrices in Eq. 6 give the correlations of the jet cross-sections in the various p_T bins, for $(R = 0.5, R = 0.5)$, $(R = 0.7, R = 0.7)$ and $(R = 0.5, R = 0.7)$ jets; the first two arise from dijet events, and the last one from the fact that a single jet can appear in both $R = 0.5$ and $R = 0.7$ categories. The B matrices in Eq. 5 then transform the covariance matrix for the data s_5 and s_7 to that for the unfolded spectra σ_5 and σ_7 . Finally, the matrix A in Eq. 4 is needed to calculate the covariance matrix U in Eq. 2 for the jet radius ratio $\mathcal{R}(0.5, 0.7)$ from those for σ_5 and σ_7 . We now describe the procedure in detail.

Most of the jets are reconstructed with both $R = 0.5$ and $R = 0.7$ clustering parameters, and often fall in the same (p_T, y) bin, resulting in strong correlation between the smeared cross sections s_5 and s_7 for $R = 0.5$ and $R = 0.7$, respectively. The size of this correlation is determined from data for adjacent p_T bin pairs by dividing events into independent subsets with jet number cross-sections m_{pq}^{ij} , based on the number q of $R = 0.5$ and p of $R = 0.7$ jets they contribute in the bins i and j , respectively. The measured correlation between s_5 and s_7 for bin $i = j$ in data is about 0.4 at $p_T = 50$ GeV, rising up to 0.65 at $p_T = 100$ GeV, and finally up to 0.85 at above

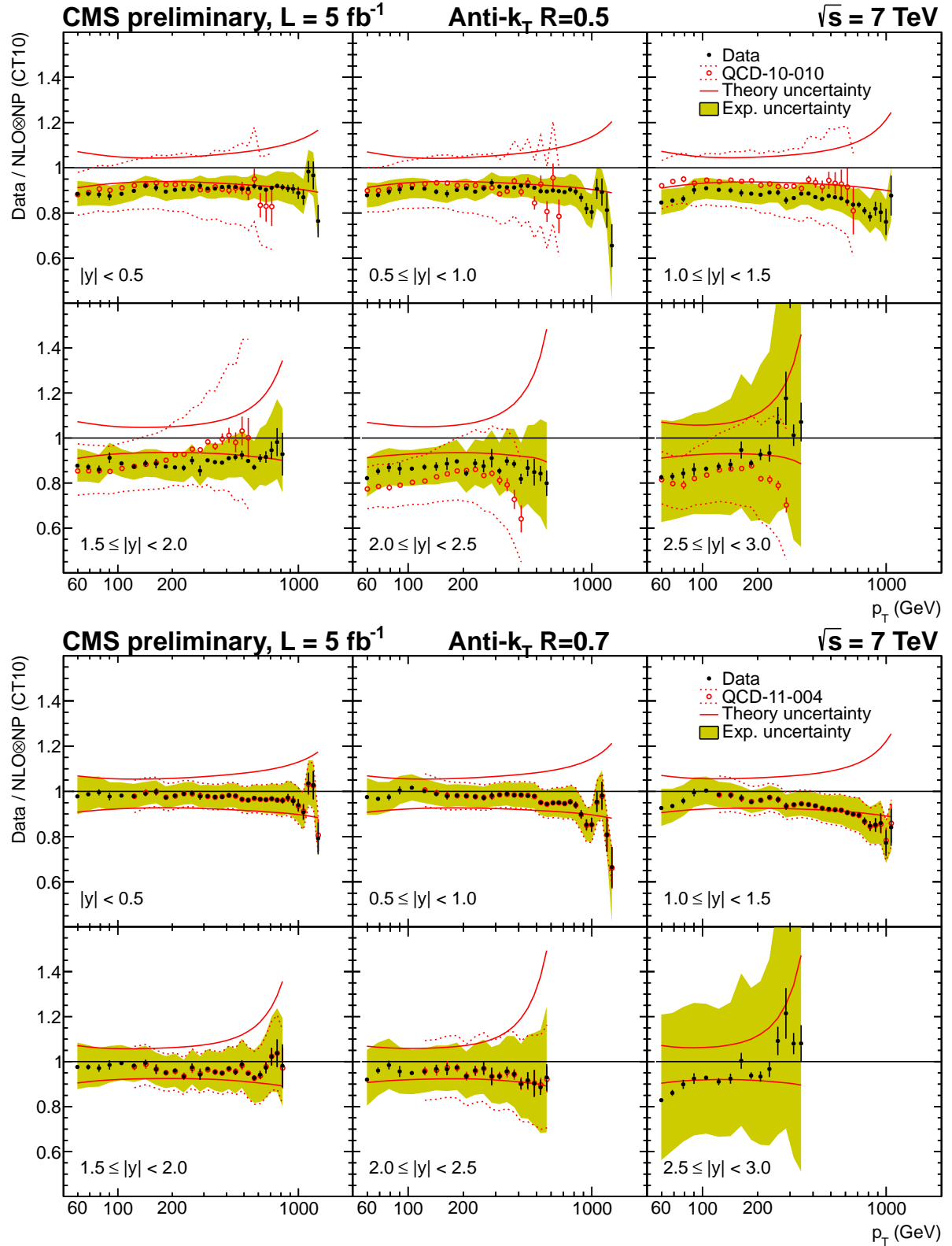


Figure 2: Inclusive jet cross section with anti- k_T $R = 0.5$ (top) and $R = 0.7$ (bottom) divided by NLO⊗NP theory prediction, and compared to previous CMS measurements with 36 pb^{-1} and 5 fb^{-1} , respectively. The statistical and systematic uncertainties are represented by the error bars and the continuous band, respectively. The solid lines outline the theory uncertainty and the dotted lines outline the systematic uncertainty for the earlier measurements.

$p_T = 1$ TeV. The correlation is almost independent of rapidity for fixed p_T . At low p_T there is fairly strong correlation of up to 0.4 between bins $i = j - 1$ and j , and of up to 0.1 between bins $i = j - 2$ and j . A small correlation of up to 0.1 between bins $i = j + 1$ and j is also observed at high p_T at $|y| < 1.0$ due to dijet events contributing jets into adjacent p_T bins. This correlation is also present for jets reconstructed with the same radius parameter, and is considered in the error propagation. The correlation between other bins is negligible.

The error propagation can be summarized in matrix notation:

$$U = AVA^T, \quad V = \begin{bmatrix} V_{55} & V_{57} \\ (V_{57})^T & V_{77} \end{bmatrix}, \quad (2)$$

$$V_{55} = B_5 W_{55} B_5^T, \quad V_{57} = B_5 W_{57} B_7^T, \quad V_{77} = B_7 W_{77} B_7^T, \quad \text{where} \quad (3)$$

$$A_{ik} = \begin{cases} \mathcal{R}_i \frac{1}{\sigma_{5,i}} & \text{if } k = i, \text{ and } i \leq n, \\ -\mathcal{R}_i \frac{1}{\sigma_{7,i}} & \text{if } k = i + n, \text{ and } i \leq n, \\ 0 & \text{otherwise,} \end{cases} \quad (4)$$

$$B_{5,ij} = \frac{\partial \sigma_{5,i}}{\partial s_{5,j}}, \quad B_{7,ij} = \frac{\partial \sigma_{7,i}}{\partial s_{7,j}}, \quad (\text{evaluated numerically}) \quad (5)$$

$$W_{55,ij} = \sum_{p,q} pq \cdot m_{5,pq}^{ij}, \quad W_{57,ij} = \sum_{p,q} pq \cdot m_{x,pq}^{ij}, \quad W_{77,ij} = \sum_{p,q} pq \cdot m_{7,pq}^{ij}. \quad (6)$$

Here $\sigma_{5,i}$ and $\sigma_{7,i}$ are the D'Agostini unfolded cross sections, $s_{5,i}$ and $s_{7,i}$ are the corresponding smeared cross sections and $\mathcal{R}_i = \sigma_{5,i}/\sigma_{7,i}$ is the jet radius ratio. The $m_{x,pq}^{ij}$, $m_{5,pq}^{ij}$ and $m_{7,pq}^{ij}$ are jet number cross-sections with given number q and p of jets in bins of i and j , respectively, for jet radius pairs $(R = 0.5, R = 0.7)$, $(R = 0.5, R = 0.5)$, and $(R = 0.7, R = 0.7)$, respectively. Only bin pairs coming from the same single jet trigger are considered correlated. For the purposes of error propagation, the s_5 and s_7 data is represented as a single $2n$ vector with s_5 at indices 1 to n and s_7 at indices $n + 1$ to $2n$. The matrix A therefore has dimensions $n \times 2n$. Eq. 2 and Eq. 3 follow from standard error propagation, as *e.g.* in Eq. 1.55 of [49]. The partial derivatives $\partial \sigma_i / \partial s_j$ in Eq. 5 are evaluated by numerically differentiating the D'Agostini unfolding. The matrices V_{55} and V_{77} agree to within about 10% of those returned by RooUnfold for $R = 0.5$ and $R = 0.7$ p_T spectra, respectively, but also account for the bin-to-bin correlations induced by dijet events.

The resulting covariance matrix U is shown in Fig. 3 for $|y| < 0.5$. The statistical uncertainty for each bin of \mathcal{R} is illustrated as the square root of the corresponding diagonal element of the covariance matrix. The strong anti-correlation observed between neighboring bins is similar to that observed for individual spectra, and is mainly an artifact of the D'Agostini unfolding. Given the relative complexity of the error propagation, the statistical uncertainties are validated using a variant of bootstrap methods, the delete- d jackknife [50], shown in Fig. 3. In this method the data is divided into ten samples, each having a non-overlapping uniformly distributed $d = 10\%$ of the events removed. The (co)variance of the differences between these samples is scaled by $(1 - d)/d = 9$ to estimate the (co)variance of the original sample. The error propagation and jackknife methods agree in all rapidity bins within the expected jackknife uncertainty of about 30%. The largest differences are observed for $p_T > 700$ GeV at $|y| < 0.5$, where jackknife uncertainty is systematically below the error propagation estimate. This effect is presumably a correlated fluctuation introduced by the regularization in the D'Agostini unfolding. This high p_T discrepancy is not seen in MC, in other rapidity bins, or when using a different set of ten samples for the jackknife.

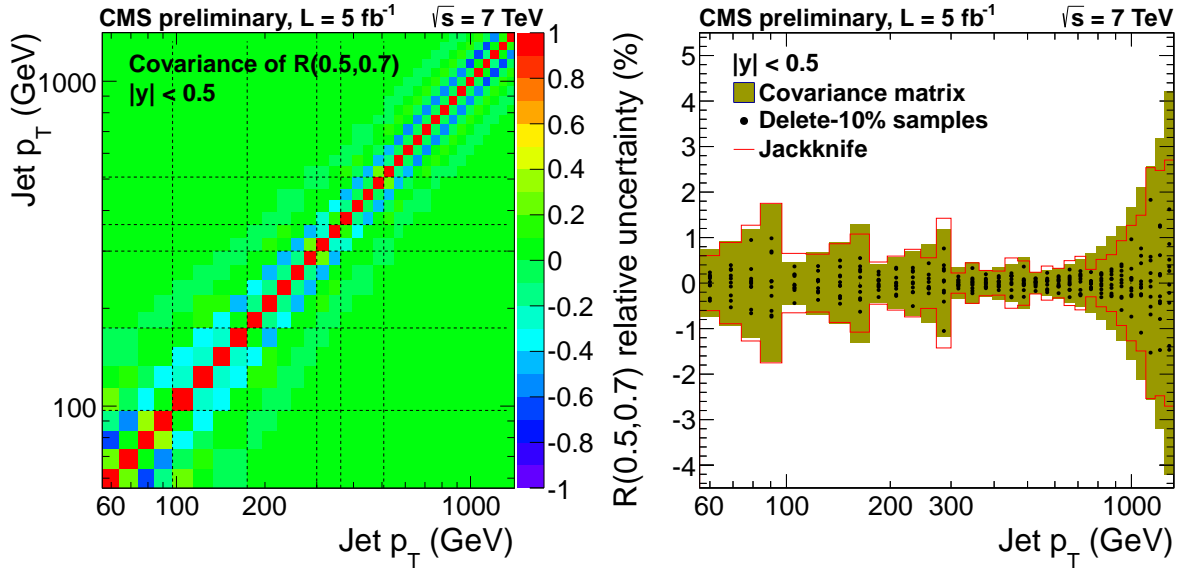


Figure 3: (Left) Covariance matrix U for the jet radius ratio R , normalized by the diagonal elements to show the level of correlation. Dashed horizontal and vertical lines indicate trigger boundaries. (Right) Comparison of the square root of the covariance matrix diagonals with a random sampling estimate using delete- d jackknife.

4.4 Experimental uncertainties

The dominant experimental uncertainties are related to the pile-up corrections and the jet p_T resolution. The total systematic uncertainty varies from about 0.4% at $p_T = 1$ TeV to 2% at $p_T = 60$ GeV within $|y| < 0.5$, and from about 1.5% at $p_T = 600$ GeV to 3.5% at $p_T = 60$ GeV within $2 < |y| < 2.5$, dominated by pile-up uncertainties. Outside tracker coverage at $2.5 < |y| < 3$ the uncertainty increases to between 3% at $p_T = 300$ GeV and 8% at $p_T = 60$ GeV. The statistical uncertainties vary from a few per mille to a couple of percent except at the very highest p_T , where they grow up to 10%.

The luminosity uncertainty, which is relevant for individual cross section measurements, cancels out in the jet radius ratio, as do most jet energy scale (JES) systematic uncertainties besides pile-up. The trigger efficiency, while almost negligible for separate cross section measurements, becomes important for the jet radius ratio when the other larger systematics cancel out and the correlations reduce the statistical uncertainty for the ratio. Other sources of systematic uncertainty, such as the jet angular resolution are negligible.

The trigger efficiency uncertainty and the quadratic sum of all almost negligible sources are assumed to be fully uncorrelated versus p_T and y . The remaining sources are assumed to be fully correlated versus p_T and y within three separate rapidity regions: barrel ($|y| < 1.5$), end cap ($1.5 \leq |y| < 2.5$) and outside tracking ($2.5 \leq |y| < 3$).

4.4.1 Pile-up uncertainty

The JES is the dominant source of systematic uncertainty for the jet cross sections, but because the $R = 0.5$ and $R = 0.7$ jets are usually reconstructed with very similar p_T , the JES uncertainty mostly cancels out in the ratio. A notable exception is the pile-up offset (PU) uncertainty, because the correction, and therefore the uncertainty, is twice as large for the $R = 0.7$ jets than for the $R = 0.5$ jets. The pile-up uncertainty is the clearly dominant systematic uncertainty in this analysis across almost all of the phase space.

The pile-up uncertainties cover the data/simulation difference observed with the data-based methods, variation in the amount of out-of-time (OOT) pile-up and the residual dependence of the jet rates per run on the mean number of primary vertices. The earlier CMS analysis [42] also included uncertainties for the offset jet p_T dependence and the resulting bias of the data-based methods observed in simulation, but these have been removed due to the good closure of the analysis in simulation when pile-up reweighting is applied separately for each trigger path.

The leading systematic uncertainty for $|y| < 2.5$ is the jet rate uncertainty, while for $|y| > 2.5$ the differences between data and simulation are dominant, with OOT variation comparable to the jet rate uncertainty. The jet rate uncertainty contributes 0.4–2% at $|y| < 0.5$ and about 1–2% $2 < |y| < 3$, with the uncertainty increasing towards lower p_T and higher rapidity. The data/MC differences contribute 0.5–1.5% at $2 < |y| < 3$ and 2–5% at $2.5 < |y| < 3$, increasing towards low p_T . They are small or negligible for lower rapidities. The OOT variation contributes less than about 0.5% in the barrel at $|y| < 1.5$, and is about the same size as the data/MC differences in the end caps within tracker coverage at $1.5 < |y| < 2.5$. Outside tracker coverage at $2.5 < |y| < 3$ the OOT variation contributes 1–2.5%, which is comparable to the residual luminosity dependence and less than the data/MC differences.

The uncertainty sources are assumed fully correlated between $R = 0.5$ and $R = 0.7$, and are simultaneously propagated to the $R = 0.5$ and $R = 0.7$ spectra before taking the jet radius ratio, one source at a time. To avoid statistical fluctuations in the systematic uncertainties, the relative uncertainties are propagated by varying the NLO \otimes NP jet p_T spectrum.

4.4.2 Unfolding uncertainty

The unfolding correction is closely related to the dependence on the jet p_T resolution (JER) and the p_T spectrum slope. For the inclusive jet p_T spectrum the relative JER uncertainty varies between 5% and 15% (30%) for $|y| < 2.5$ ($2.5 < |y| < 3$). The uncertainty in the p_T spectrum has a negligible effect for the unfolding, because the p_T binning is relatively fine and follows the jet p_T resolution.

The JER uncertainty is propagated by smearing the NLO \otimes NP cross section with smaller and larger values of JER, and comparing to the cross section smeared with the nominal JER. The relative JER uncertainty is treated as fully correlated between $R = 0.5$ and $R = 0.7$, and thus the uncertainty mostly cancels for the jet radius ratio. Some residual uncertainty remains mainly at $p_T < 100$ GeV, where the magnitude of JER differs between $R = 0.5$ and $R = 0.7$, due to additional smearing for the larger cone size from the pile-up offset. The unfolding uncertainty at $p_T = 60$ GeV varies between about 1% at $|y| < 0.5$ to 2% at $2 < |y| < 2.5$ and 5–7% at $2.5 < |y| < 3.0$. It quickly falls down to a sub-dominant uncertainty by $p_T = 100$ GeV, and is practically negligible at $p_T > 200$ GeV for all rapidity bins.

4.4.3 Trigger efficiency uncertainty

The trigger turn-ons for $R = 0.7$ are slower than for $R = 0.5$, which leads to relative inefficiencies near the trigger p_T thresholds. The trigger efficiencies are estimated in MC by applying the trigger p_T cuts on calorimeter jets, and then compared between data and MC by applying the tag-and-probe method. In this method the tag jet is required to have 100% trigger efficiency, while the unbiased particle flow probe jet is matched to a calorimeter jet to evaluate the trigger efficiency. The data/MC difference in the tag-and-probe method is taken as the trigger efficiency uncertainty, which is assumed fully uncorrelated versus p_T and y .

The peaks in trigger uncertainty are about 0.5–1.5%, and generally found for the bins with the smallest statistical uncertainty. For the other bins the trigger uncertainty is small or negligible

compared to the statistical uncertainty. Adding trigger uncertainty in quadrature with the statistical uncertainty results in total uncorrelated uncertainty of between about 0.5–2% for most p_T bins, except at the highest p_T .

5 Results

The results for the jet radius ratio $\mathcal{R}(0.5, 0.7)$ are presented in Figs. 4 in six bins of rapidity for $|y| < 3.0$. Each source of systematic uncertainty is assumed to be fully correlated between the $R = 0.5$ and $R = 0.7$ cross section measurements, which is supported by closure tests performed in simulation. The statistical uncertainty includes the correlations between $R = 0.5$ and $R = 0.7$ jets, and the correlations induced by dijet events and unfolding, propagated to the jet radius ratio. The uncorrelated systematic uncertainty from the trigger efficiency and small sources is added in quadrature with the statistical uncertainty to obtain the total uncorrelated uncertainty.

In the region corresponding to $|y| < 2.5$, the jet radius ratio does not exhibit a significant rapidity dependence. The ratio rises toward 1 with increasing p_T . The perturbative QCD predictions are systematically above the data with little rapidity dependence, but the NLO \otimes NP prediction is closer to the data than the LO \otimes NP. The pQCD predictions without non-perturbative corrections are in clear disagreement with the data. The non-perturbative effects are large at $p_T < 1000$ GeV, but they are expected to be quite reliably calculated using the latest tunes of PYTHIA 6 and HERWIG++, for which the non-perturbative corrections agree reasonably well. In the $|y| < 2.5$ region the measurement takes advantage of the presence of the tracker, which reduces the overall systematic uncertainties. The jet energy calibration procedure introduces a strong correlation among different y bins at $|y| < 1.5$ and $1.5 < |y| < 2.5$. In contrast, the region $2.5 < |y| < 3$ relies mainly on the calorimeters and suffers from larger systematic uncertainties. There the systematic uncertainty exceeds the difference between the data and the theory.

In Fig. 5 the data are compared to the different Monte Carlo predictions. The best agreement is reached with the POWHEG predictions. Comparing the parton showering predictions of PYTHIA 6 and HERWIG++ to data shows agreement across parts of the phase space, and disagreement in other places. PYTHIA 6 tune Z2 agrees well with data at the low p_T end of the measurement, where non-perturbative effects dominate. This is where PYTHIA benefits most from having been tuned to the LHC underlying event data. HERWIG++ on the other hand is in disagreement with the low p_T data, which is expected to be primarily due to the much worse underlying event tune in HERWIG. This disagreement between the underlying event in data and HERWIG++ has been directly verified e.g., by observing that for the same pile-up conditions the energy density ρ [51] is larger by 0.3 GeV in HERWIG than in data, while PYTHIA describes well the energy density in data. At higher p_T the situation is reversed, with HERWIG++ agreeing well with data and PYTHIA 6 disagreeing. In this part of the phase space it would seem that the HERWIG++ parton shower model, which also accounts for color reconstructions, is superior to the Lund string model used in PYTHIA. This fact might be related to the better ability of HERWIG to describe the high p_T jet substructure with respect to PYTHIA [52].

In summary this measurement shows the importance of the higher order corrections for the jet cross sections measured with a small radius such as $R = 0.5$. Those correction are well accounted for by the parton showering models and more particularly by the FSR [53].

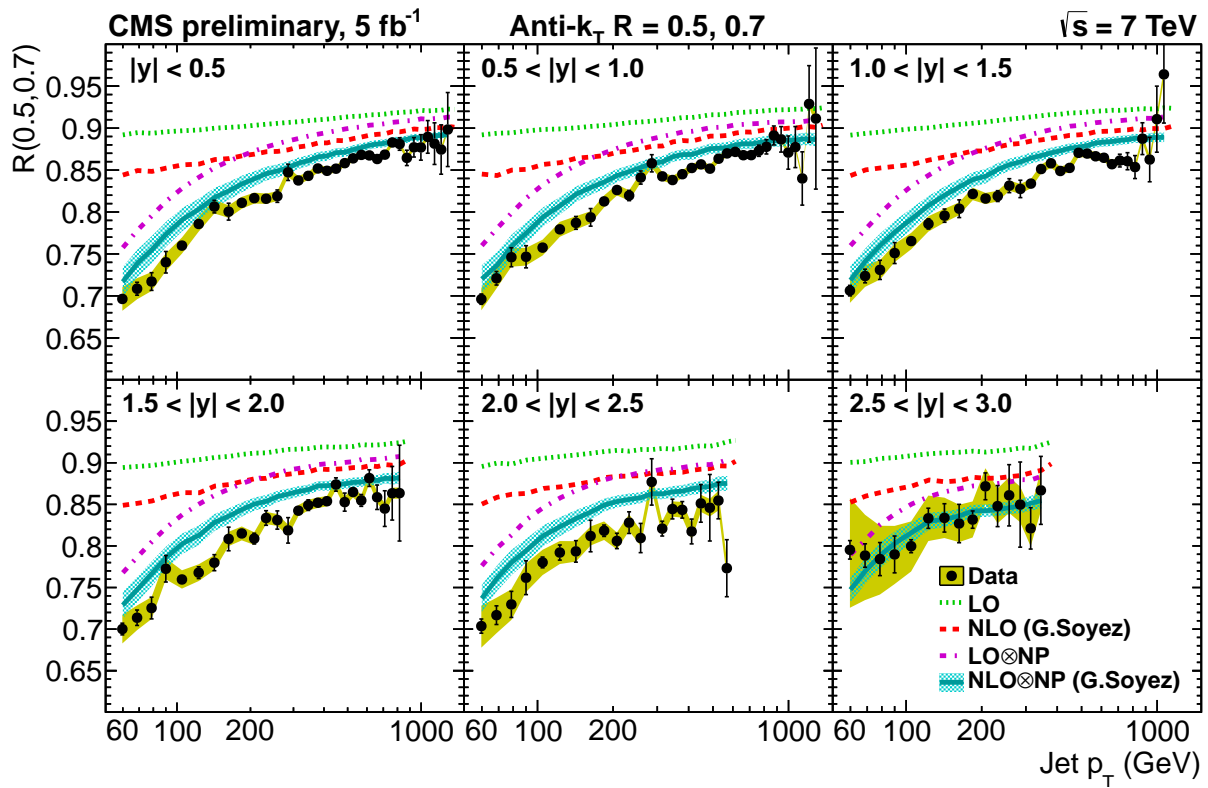


Figure 4: Jet radius ratio $\mathcal{R}(0.5,0.7)$ in six rapidity bins up to $|y| < 3.0$, compared to pQCD predictions. The bands shows the total correlated systematic uncertainty, the error bars the total uncorrelated uncertainty, and the horizontal ticks the statistical uncertainty.

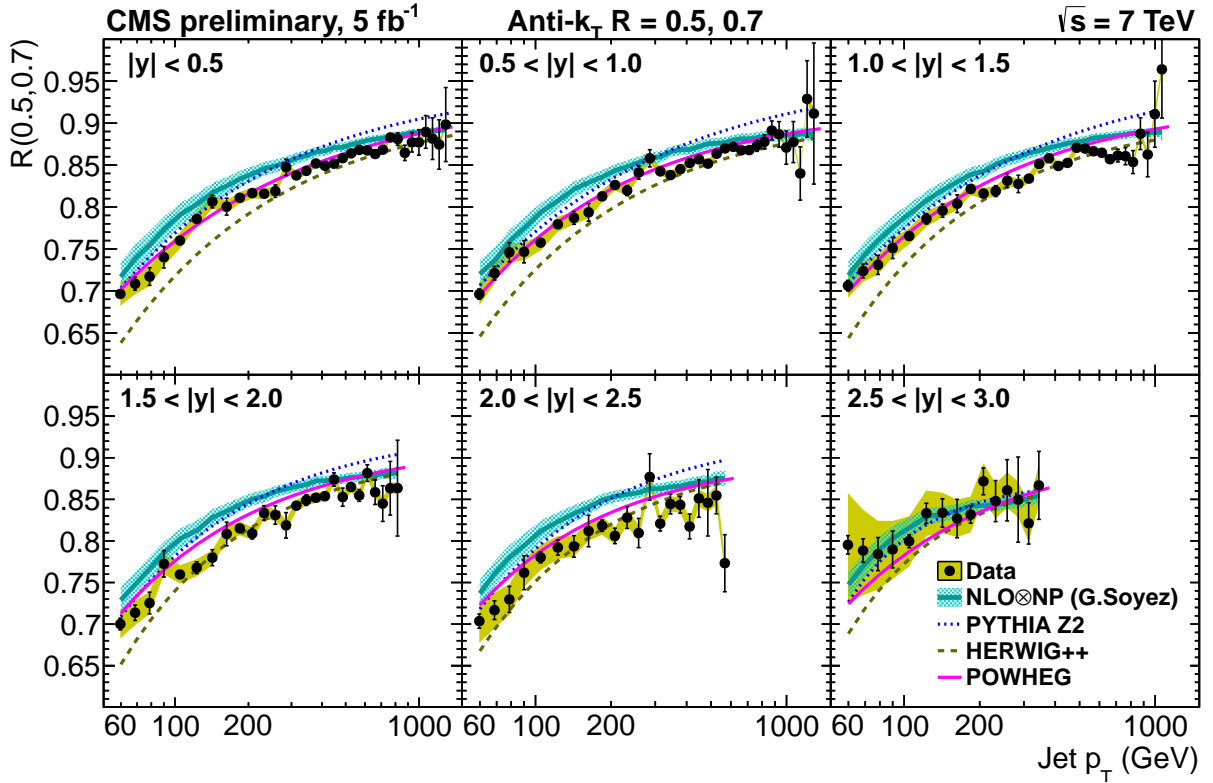


Figure 5: Jet radius ratio $\mathcal{R}(0.5, 0.7)$ in six rapidity bins up to $|y| < 3.0$, compared to NLO \otimes NP and MC predictions. The bands shows the total correlated systematic uncertainty, the error bars the total uncorrelated uncertainty, and the horizontal ticks the statistical uncertainty.

6 Conclusions

The jet radius ratio $\mathcal{R}(0.5, 0.7)$ was measured as function of rapidity y and transverse momentum p_T . The models using LO or NLO matrix element calculations matched to the parton showers better describe the ratio than the fixed order calculations corrected for non-perturbative effects. This observation holds for all the region with $|y| < 2.5$ independent of y . At $|y| > 2.5$ the experimental uncertainty limits the ability to discriminate different predictions.

This study exhibits collinear radiation as one of the sources which leads to systematic discrepancies between the fixed order calculations and the measurements of the inclusive jet spectrum at small radius parameters ($R \leq 0.5$). This result combined to the absolute measurements of the jet cross sections tends to indicate that a larger radius is preferable to use for the jet cross section in the PDF and α_s fits. More precisely if fixed order calculations at NLO corrected for the non-perturbative effects are used, a larger radius tend to reduce the significant missing order corrections which are well described by the parton showering models.

The optimal size of the radius is a trade-off between the reduction of losses due to the collinear radiation ($|\ln R|$), the reduction of the non-perturbative effects ($1/R$) from one side and the reduction of the amount of collected pile-up and underlying event energy (R^2) on the other [54].

The analyses where large cone sizes are not practical, e.g. top physics measurements or heavy ions, may benefit from the use of NLO matched to parton showers as in POWHEG.

References

- [1] Z. Nagy, “Next-to-leading order calculation of three jet observables in hadron hadron collision”, *Phys.Rev.* **D68** (2003) 094002, doi:10.1103/PhysRevD.68.094002, arXiv:hep-ph/0307268.
- [2] A. Gehrmann-De Ridder et al., “Jet rates in electron-positron annihilation at $\mathcal{O}(\alpha_s^3)$ in QCD”, *Phys.Rev.Lett.* **100** (2008) 172001, doi:10.1103/PhysRevLett.100.172001, arXiv:0802.0813.
- [3] G. Dissertori et al., “Precise determination of the strong coupling constant at NNLO in QCD from the three-jet rate in electron-positron annihilation at LEP”, *Phys.Rev.Lett.* **104** (2010) 072002, doi:10.1103/PhysRevLett.104.072002, arXiv:0910.4283.
- [4] H1 Collaboration, “Jet Production in ep Collisions at High Q^2 and Determination of $\alpha(s)$ ”, *Eur.Phys.J.* **C65** (2010) 363–383, doi:10.1140/epjc/s10052-009-1208-7, arXiv:0904.3870.
- [5] ZEUS Collaboration, “Jet-radius dependence of inclusive-jet cross-sections in deep inelastic scattering at HERA”, *Phys.Lett.* **B649** (2007) 12–24, doi:10.1016/j.physletb.2007.03.039, arXiv:hep-ex/0701039.
- [6] S. Sjostrand, T. Mrenna and S. P., “PYTHIA 6.4 physics and manual”, *J. High Energy Phys.* **0605** (2006) 026.
- [7] M. Bahr et al., “HERWIG++ Physics and Manual”, *Eur. Phys. J.* **C58** (2008) 639–707.
- [8] B. Andersson and A. Nilsson, “Revisiting the Lund fragmentation model”, technical report, (1992).

- [9] B. Webber, “A QCD model for jet fragmentation including soft gluon interference”, *Nuclear Physics B* **238** (1984), no. 3, 492 – 528, doi:10.1016/0550-3213(84)90333-X.
- [10] N. Brown and W. J. Stirling, “Finding jets and summing soft gluons: A New algorithm”, *Z.Phys.* **C53** (1992) 629–636, doi:10.1007/BF01559740.
- [11] G. P. Cacciari, M. Salam *Phys. Lett. B* **641** (2006) 57.
- [12] CDF Collaboration, “Measurement of the Inclusive Jet Cross Section using the k_T algorithm in $p\bar{p}$ collisions at $\sqrt{s} = 1.96$ TeV with the CDF II Detector”, *Phys.Rev.* **D75** (2007) 092006, doi:10.1103/PhysRevD.75.092006, arXiv:hep-ex/0701051.
- [13] CDF Collaboration, “Measurement of the Inclusive Jet Cross Section at the Fermilab Tevatron p anti-p Collider Using a Cone-Based Jet Algorithm”, *Phys.Rev.* **D78** (2008) 052006, doi:10.1103/PhysRevD.78.052006, arXiv:0807.2204.
- [14] D0 Collaboration, “Measurement of the inclusive jet cross-section in $p\bar{p}$ collisions at $\sqrt{s} = 1.96$ TeV”, *Phys.Rev.Lett.* **101** (2008) 062001, doi:10.1103/PhysRevLett.101.062001, arXiv:0802.2400.
- [15] D0 Collaboration, “Measurement of the inclusive jet cross section in $p\bar{p}$ collisions at $\sqrt{s} = 1.96$ TeV”, *Phys.Rev.* **D85** (2012) 052006, doi:10.1103/PhysRevD.85.052006, arXiv:1110.3771.
- [16] G. C. Blazey et al., “Run II jet physics”, arXiv:hep-ex/0005012.
- [17] S. Ellis et al., “Jets in hadron-hadron collisions”, *Prog.Part.Nucl.Phys.* **60** (2008) 484–551, doi:10.1016/j.ppnp.2007.12.002, arXiv:0712.2447.
- [18] CMS Collaboration, “Measurement of the Inclusive Jet Cross Section in pp Collisions at $\sqrt{s} = 7$ TeV”, *Phys.Rev.Lett.* **107** (2011) 132001, doi:10.1103/PhysRevLett.107.132001, arXiv:1106.0208.
- [19] CMS Collaboration Collaboration, “Measurements of differential jet cross sections in proton-proton collisions at $\sqrt{s} = 7$ TeV with the CMS detector”, *Phys.Rev.* **D87** (2013) 112002, doi:10.1103/PhysRevD.87.112002, arXiv:1212.6660.
- [20] S. Chatrchyan et al., “Measurement of the inclusive production cross sections for forward jets and for dijet events with one forward and one central jet in pp collisions at $\sqrt{s} = 7$ TeV.”, *J. High Energy Phys.* **06** (Feb, 2012) 036.
- [21] ATLAS Collaboration, “Measurement of inclusive jet and dijet production in pp collisions at $\sqrt{s} = 7$ TeV using the ATLAS detector”, *Phys.Rev.* **D86** (2012) 014022, doi:10.1103/PhysRevD.86.014022, arXiv:1112.6297.
- [22] ATLAS Collaboration, “Measurement of the inclusive jet cross section in pp collisions at $\sqrt{s} = 2.76$ TeV and comparison to the inclusive jet cross section at $\sqrt{s} = 7$ TeV using the ATLAS detector”, Technical Report ATLAS-CONF-2012-128, CERN, Geneva, (Sep, 2012).
- [23] ALICE Collaboration, “Measurement of the inclusive differential jet cross section in pp collisions at $\sqrt{s} = 2.76$ TeV”, arXiv:1301.3475.
- [24] S. Frixione, P. Nason, and C. Oleari, “Matching NLO QCD computations with Parton Shower simulations: the POWHEG method”, *JHEP* **0711** (2007) 070, doi:10.1088/1126-6708/2007/11/070, arXiv:0709.2092.

- [25] CMS Collaboration, “Dijet Azimuthal Decorrelations in pp Collisions at $\sqrt{s} = 7$ TeV”, *Phys.Rev.Lett.* **106** (2011) 122003, doi:10.1103/PhysRevLett.106.122003, arXiv:1101.5029.
- [26] ATLAS Collaboration, “Measurement of Dijet Azimuthal Decorrelations in pp Collisions at $\sqrt{s} = 7$ TeV”, *Phys.Rev.Lett.* **106** (2011) 172002, doi:10.1103/PhysRevLett.106.172002, arXiv:1102.2696.
- [27] CMS Collaboration, “Shape, transverse size, and charged hadron multiplicity of jets in pp collisions at 7 TeV”, *JHEP* **1206** (2012) 160, doi:10.1007/JHEP06(2012)160, arXiv:1204.3170.
- [28] ATLAS Collaboration, “Study of Jet Shapes in Inclusive Jet Production in pp Collisions at $\sqrt{s} = 7$ TeV using the ATLAS Detector”, *Phys.Rev.* **D83** (2011) 052003, doi:10.1103/PhysRevD.83.052003, arXiv:1101.0070.
- [29] CMS Collaboration, “The CMS experiment at the CERN LHC”, *JINST* **0803** (2008) S08004.
- [30] G. Marchesini and B. Webber *Nucl. Phys.* **B310** (1998) 461.
- [31] I. Knowles *Nucl. Phys.* **B310** (1998) 571.
- [32] I. Knowles *Comput. Phys. Commun.* **58** (1990) 271.
- [33] R. Field, “Early LHC underlying event data - findings and surprises”, arXiv:1010.3558.
- [34] B. Pumplin et al., “New generation of parton distributions with uncertainties from global QCD analysis”, *J. of High Energy Phys.* **07** (2002) 012.
- [35] B. Anderson *Phys. Rep.* **97** (1983) 31.
- [36] T. Sjostrand *Phys. Lett.* **B142** (1984) 420.
- [37] P. Nason, “A New method for combining NLO QCD with shower Monte Carlo algorithms”, *JHEP* **0411** (2004) 040, doi:10.1088/1126-6708/2004/11/040, arXiv:hep-ph/0409146.
- [38] S. Alioli et al., “A general framework for implementing NLO calculations in shower Monte Carlo programs: the POWHEG BOX”, *JHEP* **1006** (2010) 043, doi:10.1007/JHEP06(2010)043, arXiv:1002.2581.
- [39] J. Butterworth, J. R. Forshaw, and M. Seymour, “Multiparton interactions in photoproduction at HERA”, *Z.Phys.* **C72** (1996) 637–646, doi:10.1007/s002880050286, arXiv:hep-ph/9601371.
- [40] T. Kluge, K. Rabbertz, and M. Wobisch, “FastNLO: Fast pQCD calculations for PDF fits”, arXiv:hep-ph/0609285.
- [41] G. Soyez, “A Simple description of jet cross-section ratios”, *Phys.Lett.* **B698** (2011) 59–62, doi:10.1016/j.physletb.2011.02.061, arXiv:1101.2665.
- [42] CMS Collaboration, “Measurement of the Inclusive Jet Cross Section in pp Collisions at $\sqrt{s} = 7$ TeV”, *Phys.Rev.Lett.* **107** (2011) 132001, doi:10.1103/PhysRevLett.107.132001, arXiv:1106.0208.

- [43] CMS Collaboration, “Particle–Flow Event Reconstruction in CMS and Performance for Jets, Taus, and E_T^{miss} ”, *CMS Physics Analysis Summary CMS-PAS-PFT-09-001* (2009).
- [44] C. Collaboration, “Determination of jet energy calibration and transverse momentum resolution in CMS”, *JINST* **6** (2011) P11002.
- [45] G. P. Cacciari, M. Salam and G. Soyez, “The anti- k_t jet clustering algorithm”, *J. High Energy Phys.* **04** (2008) 063.
- [46] M. Cacciari, G. P. Salam, and G. Soyez, “”, <http://www.fastjet.fr>.
- [47] T. Adye, “Unfolding algorithms and tests using RooUnfold”, [arXiv:1105.1160](https://arxiv.org/abs/1105.1160).
- [48] G. D’Agostini, “A Multidimensional unfolding method based on Bayes’ theorem”, *Nucl. Instrum. Meth* **A362** (1995).
- [49] G. Cowan, “Statistical data analysis”. Oxford University Press, USA, 1998.
- [50] B. Efron and R. Tibshirani, “An introduction to the bootstrap”. Monographs on statistics and applied probabilities. Chapman & Hall/CRC, 1993.
- [51] M. Cacciari and G. P. Salam, “Pileup subtraction using jet areas”, *Phys.Lett.* **B659** (2008) 119–126, [doi:10.1016/j.physletb.2007.09.077](https://doi.org/10.1016/j.physletb.2007.09.077), [arXiv:0707.1378](https://arxiv.org/abs/0707.1378).
- [52] CMS Collaboration, “Search for heavy resonances in the W/Z-tagged dijet mass spectrum in pp collisions at 7 TeV”, [arXiv:1212.1910](https://arxiv.org/abs/1212.1910).
- [53] G. Soyez, “Optimal jet radius in kinematic dijet reconstruction”, *J. High Energy Phys.* **07** (Jun, 2010) 075. Comments: 30 pages, 11 figures.
- [54] M. Dasgupta, L. Magnea, and G. P. Salam, “Non-perturbative QCD effects in jets at hadron colliders”, *JHEP* **0802** (2008) 055, [doi:10.1088/1126-6708/2008/02/055](https://doi.org/10.1088/1126-6708/2008/02/055), [arXiv:0712.3014](https://arxiv.org/abs/0712.3014).